

# State of the art experimental apparatus for fast entangling gates in trapped multi-ion crystals

Donovan Webb

Department of Physics, University of Oxford

E-mail: [donovan.webb@physics.ox.ac.uk](mailto:donovan.webb@physics.ox.ac.uk)

## Abstract.

Scalable trapped-ion quantum computation relies on the development of high-fidelity fast entangling gates in many-ion crystals. Currently the speed of Mølmer-Sørensen entangling gates is limited by off-resonant carrier excitations which do not commute with the necessary sideband excitations. Standing waves formed by counter-propagating lasers offer a potential pathway to achieve fast entanglement by suppressing undesired carrier excitations. We present initial results of this carrier suppression in the 674-nm quadrupole transition of  $^{88}\text{Sr}^+$ . We demonstrate fast two-qubit entangling gates which exceed the entangling “speed limit” imposed by non-commuting off-resonant carrier excitations. To explore entangling operations at durations comparable to the secular trap frequency we require high intensity laser addressing. A new system is being constructed featuring standing wave single ion addressing to generate these high intensities. It will also utilize a microfabricated, segmented 3D Paul trap for greater control of long ion chains. We will use  $^{40}\text{Ca}^+$  which has a quadrupole transition at 729-nm. We present the current progress and roadmap of this next-generation platform and motivations behind the design choices.

## 1. Introduction

Ion traps, specifically Paul and Penning traps [1, 2], have enabled the experimental exploration and corroboration of atomic and quantum theory, with applications in metrology [3] and quantum simulation [4].

With the high degree of experimental control of a quantum system exhibited by ion trap systems, they are a promising and increasingly mature platform for enabling Quantum Computation (QC) [5].

Errors in quantum logic gates due to noise and decoherence of the physical qubits are inevitable and limit algorithm circuit depths. With error correction [6] schemes this depth can be greatly extended but requires a large overhead of qubits and operations, which at current scales is not practical. Noisy intermediate scale QC (NISQ) [7], an alternative to error corrected QC, is only practical when individual gate fidelities (1 - gate errors) are sufficiently low. The ion trap platform is a leading candidate for NISQ with state-of-the-art fidelities for both single- and two-qubit gates [8–10]. Entangling gates are a necessity for universal QC [11, 12], and also have applications in enhanced

sensing and metrology [13, 14]. However the relatively long two-qubit entangling durations in ion traps limits both the fidelity of two qubit gates, and the overall circuit depth of an algorithm possible with a “wall clock” time below  $\tau_0$ , the qubit coherence time.

Here, we shall discuss a possible route to fast two-qubit entangling gates, report on initial results from a proof of principle experiment, and describe a new ion trap apparatus being constructed tailored for exploring entanglement on the timescale of the ion motion.

Two electronic energy levels within the ion are used to define our qubit spin states while the trapping potential leads to multiple motional (Fock) states of the ion crystal [2]. To entangle the spins of two ions within the crystal we may use these common modes of motion as a quantum information bus. This is achieved by a spin dependent coupling of the ion’s spin with a motional mode of the crystal. The duration of this applied spin dependent force is set so the motion returns to the original Fock state and the spin states acquire different phases, effectively transferring from spin-motion to spin-spin entanglement. One such implementation of this method, the Mølmer-Sørensen gate (MS-gate) [15], uses a travelling bichromatic field of either lasers or microwaves detuned symmetrically from the qubit (carrier) resonance. The two fields off resonantly drive this motion (sideband transitions), to create a spin dependent force. XXnote on fastgates [16, 17]XX. However, also present in the MS-interaction is off resonant driving of the carrier transition. This unwanted carrier term becomes the leading source of error at short gate durations [18]. To overcome this limitation we may use a standing bichromatic field to suppress the off resonant driving of the carrier. The carrier interaction in an electronic quadrupole transition couples to the gradient of the E field, whilst the sideband couples to the curvature. The use of a standing wave phase stabilised with respect to the ion gives a positional dependence of both the gradient and curvature of the electric field. If the ions are placed at a point in the standing wave of zero gradient, the off resonant carrier coupling in the MS-interaction is suppressed.

## 2. Carrier Nulling Results

Here, we report experimental results of both standing wave (SW) single-qubit gates and SW Mølmer-Sørensen entangling gates with the carrier term suppressed [18].

These experiments were performed on our “Blade” apparatus [17, 19] which, although suitable for this proof-of-principle work, has hard limitations on what gate durations can be achieved due to available laser power and only global addressing of the ions. Section 3 will further discuss these limitations and the solution in the form of a new ion trap apparatus.

On “Blade” the SW is formed by two superimposed counter-propagating 674-nm beams and directed onto the ions at an angle of  $45^\circ$  to the ion chain, Figure 1 (a). 674-nm light couples to the quadrupole qubit transition,  $5S_{1/2} \Leftrightarrow 4D_{5/2}$ , in  $^{88}\text{Sr}^+$ . The

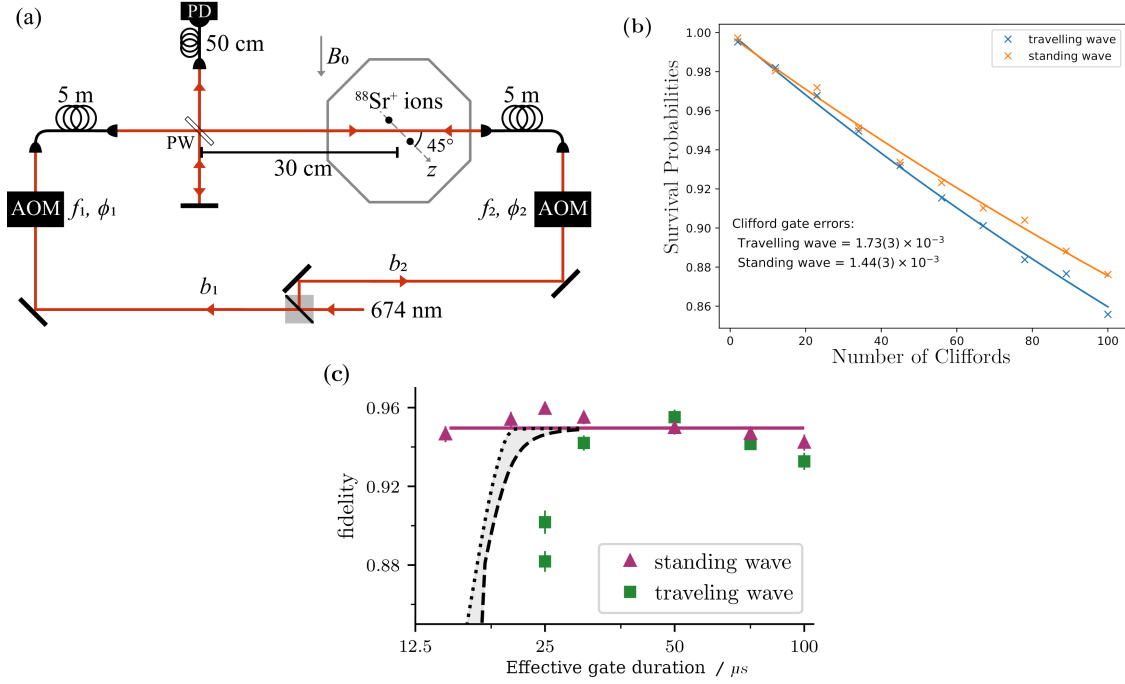


**Figure 1.** Proof-of-principle experiments of using standing waves for single- and two-qubit gates[18]. **a)** A schematic of the beam path arrangement to form a standing wave at the ions. Incoming 674-nm light is split into two branches,  $b_1$  and  $b_2$ . AOMs control the frequency and phase of these two branches. The light is directed onto the  $^{88}\text{Sr}^+$  ions at an angle of  $45^\circ$ . Picked off light from both branches interfere at a photodetector (PD) and an error signal is generated to phase stabilise the standing wave. **b)** Single qubit random benchmarking results for both travelling and standing waves. A decay model (solid line) is fitted to find both state-prepare and Clifford gate errors. **c)** The fidelity of MS entangling gates as gate duration is reduced. It can be seen that the travelling wave fidelity drops rapidly at short gate durations whilst the standing wave fidelity remains at 0.95.

beams propagate in free-space and are phase-stabilized to ensure the SW is stationary with respect to the ion. AOMs in both branches are used as switches, to apply sideband frequencies, and to control the phase of the beams.

### 2.1. Random Benchmarking

High fidelity unitary operations (gates) are essential for both near intermediate scale quantum computing and for reducing overheads in required physical qubits and operations in fault-tolerant schemes [6]. To evaluate whether the phase stability of our SW is sufficient for high fidelity gates, we employ randomized benchmarking (RBM) [20, 21]. RBM consists of applying random combinations of a pre-chosen discrete set of gates to estimate an average error per gate. We chose the single-qubit Clifford group as our set of gates to evaluate. The single-qubit Clifford group is the set of unitaries which map

the Pauli matrices to one another through conjugation. This can be thought of as the complete set of rotations of the Bloch sphere such that all valid combinations of the axis ( $x \rightarrow \{\pm x, \pm y, \pm z\}$ ), ( $y \rightarrow \{\pm x, \pm y, \pm z\}$ ), ( $z \rightarrow \{\pm x, \pm y, \pm z\}$ ) are realized. There are 24 unitaries in this set. We followed the RBM protocol described in the Thesis [22] to evaluate our SW single-qubit gates. First the qubit is prepared in some known initial state, i.e. prepared in some chosen basis. A gate sequence is then applied which consists of multiple random Clifford gates followed by a final ‘inverting’ Clifford, where the ‘inverting’ Clifford is chosen such that the full sequence performs the Identity operation. The state is then measured in the same basis to find any deviations from the Identity being performed due to gate errors. This is repeated with the same preparation and sequence multiple times to calculate the probability that the Identity was performed - thus giving the sequence fidelity. These steps are repeated for many different random sequences with a range of sequence lengths. The sequence fidelity versus number of Clifford gates performed has now been found and a decay model is fitted to find the both the error per Clifford and the state preparation error.

Using this method we compared the single-qubit gate errors when utilizing either standing or travelling waves. We obtained an error of  $1.44(3) \times 10^{-3}$  and  $1.73(3) \times 10^{-3}$  per Clifford gate for the SW and travelling single-qubit gates, respectively, seen in Figure 1 (b). Thus, use of the SW, and the added experimental complexity it entails, is not detrimental to single-qubit gate fidelity. Due to spin dephasing of our quadrupole qubit originating from laser noise, external field noise and the natural lifetime of the transition, we took care to ensure that the duty cycle and Rabi frequency of both SW and travelling wave RBM experiments were the same.

## 2.2. Standing wave Mølmer-Sørensen

To explore two-qubit entangling gates we implement an MS-type scheme with a bichromatic SW and compare with the conventional bichromatic travelling wave (TW). The bichromatic field is created by applying two tones to the AOMs in Figure 1 (a). As with the TW MS-scheme, these tones are symmetrically detuned by  $\delta \approx \pm(\omega_z + \delta_g)$  from the qubit resonance. Here  $\omega_z$  is the axial mode frequency of our trapped single ion,  $\omega_z = 2\pi \times 1.2$  MHz, and  $\delta_g$  is some further detuning from these sidebands. To selectively couple to the sidebands, and hence suppress the carrier term, the ion spacing is adjusted to place them both on antinodes of the bichromatic SWs.

In Figure 1 (c), we show the two-qubit fidelities achieved with the two schemes as a function of the effective gate duration ( $2\pi/\delta_g$ , where  $\delta_g = \delta - \omega_z$ ). For slower gates, the fidelity of the SW-MS is comparable with that of the TW-MS. For faster entangling gates, the fidelity of the TW-MS degrades rapidly as expected due to the carriers presence. In contrast, the fidelity for the SW-MS is consistent with  $\approx 0.95$  over the entire available power range, showing that we have eliminated the limit arising from the carrier coupling. The shortest SW-MS gate was 15  $\mu$ s, limited by the achievable intensity of

light at the ion in this ion-trap apparatus.

As gate duration is inversely proportional to the required Rabi frequency to complete an entangling gate, we can further increase the speed of these gates using greater intensities of light at the ions. This can be achieved by more powerful lasers or by focusing the beams down to tighter waists at the ions locations. The current apparatus is limited to global addressing with a large waist beam and the laser power at 674-nm cannot be practically increased. Therefore, to explore these faster gates a new apparatus has been designed and is being constructed with the ability to create tight waist standing waves at the ion position. Further, a state-of-the-art trap allows exploration of these gates in many ion crystals. A description and progress report of this system is described in the following section.

### 3. Experimental Apparatus

The technical complexity of ion trapping experiments may be reduced to solving two problems: controlling the state of the ion (both internal and motional); and controlling the ion’s surrounding environment. Our ion trap experiments consist of: an atomic source, a trap, a vacuum system encasing these, external magnetic field coils, and lasers for ionization, cooling, repumping, state preparation, coherent control and readout.

Here we describe both the older generation apparatus, referred to as “Blade”, where the proof-of-principle fast gate schemes have been tested [16, 18], and the new proposed system known as “FastGates”, which solves critical limitations for further exploring fast entanglement.

#### 3.1. Ion

Singly-charged Group 2 elements are popular in ion trap experiments due to their single outer electron with Hydrogen-like energy levels. For “FastGates” we will use  $^{40}\text{Ca}^+$ .

$^{40}\text{Ca}^+$  has no nuclear spin giving the (relatively) simple level structure shown in Figure 2. An external magnetic field of 5 G is applied to split the levels via the Zeeman effect. The relevant laser transitions for our planned ion trap experiment have been marked.

A zero nuclear spin isotope of calcium was chosen due to this simple level structure without hyperfine splitting. The greater number of levels due to hyperfine splitting lead to more decay paths and therefore greater complications in both cooling and gate schemes. However, the combination of Zeeman and hyperfine splitting causes certain transitions, known as “clock”-qubits, to be robust against magnetic field fluctuations. Our lack of “clock”-qubit for initial experiments will be mitigated by suppressing field fluctuations using magnetic shielding constructed from two layers of 3 mm thick MuMetal. Further, to generate a stable 5 G field we use a permanent magnet array which has a lower temperature dependence on field strength than coils.

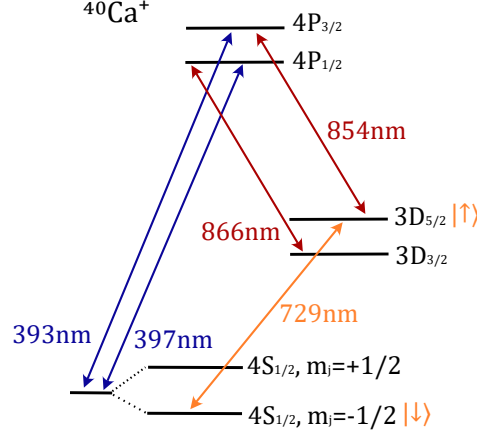


**Figure 2.** Electronic energy levels of  $^{40}\text{Ca}^+$ , which will be used in the “FastGates” experiment. The levels are split by the Zeeman effect due to a 5 G external magnetic field. The transitions marked are required for cooling and control over the ion. We shall use the optical-qubit with a quadrupole transition at 729-nm.

The natural lifetime of the metastable  $3\text{D}_{5/2}$  is around  $\tau = 1.1$  s [23], giving a favorable fundamental limit of coherence time for our chosen qubit. This natural lifetime leads to a narrow  $4\text{S}_{1/2} \Leftrightarrow 3\text{D}_{5/2}$  transition linewidth,  $\Gamma = 1/\tau < 1$  Hz, and so demands the use of a narrow linewidth laser, which is discussed in the *Laser systems* subsection.

Trap	$d / \mu\text{m}$	$\omega_{ax}, \omega_{rad} / (2\pi\text{MHz})$	$\dot{n}/qs^{-1}$	Trap depth / meV
Blade	500	1.9, 4	75	1000
HOA2	68	1.8, 2.5	2000	150
NPL	250	1.6*, 5.0*	<100	400*

**Table 1.** Comparison of different trap types at typical operating parameters. Blade is a macro blade style trap, HOA2 is a surface style trap, and NPL is a microfabricated 3D trap.  $d$  is the ion-electrode distance,  $\omega$  are the motional mode frequencies for one ion, and  $\dot{n}$  is the heating rate in quanta per second. NPL starred values are from simulation. Values for Blade and HOA2 came from [17, 22] and [24, 25] respectively.

### 3.2. Trap

To create the trapping potentials we use linear Paul traps, a schematic of such is shown in Figure 3 (a). As explained by Earnshaw’s theorem, ( $\nabla^2 V = 0$ ), a stable stationary point in 3D can not be realized using only static electric potentials,  $V$ , as if the potential is confining in two dimensions, it will be anticonfining in the third. Therefore, to achieve stable trapping an oscillating field must be utilized to create a pseudopotential. A Paul trap achieves this through an oscillating RF electric field providing radial confinement and a static field to create axial confinement. A Blade trap, Figure 3 (a), as is used in the “Blade” apparatus, has axial confinement created by DC end caps and radial

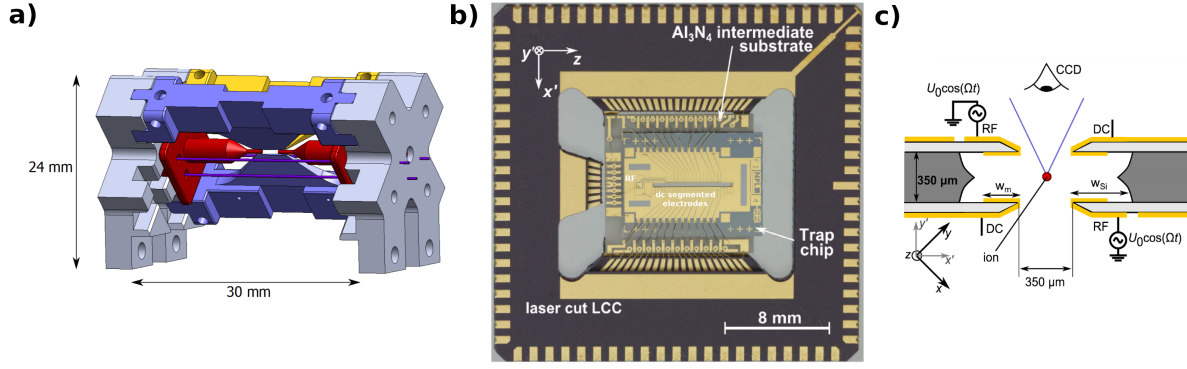


**Figure 3.** a) The blade trap used for the carrier nulling proof-of-principle experiment. In blue are the RF blades providing the radial pseudopotential whilst in red are the DC end caps providing the axial potential. b) The NPL trap to be used in the “FastGates” experiment. This is a microfabricated, segmented, multilayer trap. c) A cross sectional view of the NPL trap showing the RF and DC electrode positions. Figures from [26]. and [27].

confinement by supplying an oscillating RF voltage to the blades. In “Blade” the ion endcap distance is 1.15 mm, and ion-blade distance is 0.5 mm. Typical operating frequency for the RF electrodes of the “Blade” trap are 28.0133 MHz leading to an axial ion frequency of 1.860 MHz and radial frequencies of 4.077 MHz and 4.341 MHz. Recently, the surface style linear Paul trap has gained popularity due to the maturity of chip fabrication technologies [28] and the potential route to scalability this offers. In the surface trap, the 3D blade and endcap geometry of the “macro” trap is effectively projected onto a 2D surface. The stable point of such a trap is typically on the order of  $50 \mu\text{m}$  from the chip surface. The ease of fabrication of surface traps has allowed the creation of complex multizone devices with many DC electrodes. These multizone traps enable the shuttling of ions, a requirement for Quantum CCD type architectures [29]. However, this surface style geometry greatly reduces the depth of the trapping potential and the close proximity of the surface to the ion is a large contributor to anomalous heating [30]. Values for a widely used surface style trap, HOA2 [31], are summarised in table 1.

A microfabricated 3D trap [32, 33], as will be used in the “FastGates” apparatus, brings together the advantages of chip fabrication as well as low heating rates and high trapping depths of a 3D style trap with greater ion-surface distances. This is achieved by a multilayer chip as shown in Figure 3 (b, c). The radial trapping is provided by RF rails on opposite diagonals of the slit whilst axial trapping may be realized by DC electrodes. The ion-surface distance is now of the order  $250 \mu\text{m}$  and the heating rates have been shown to be  $< 100 \text{ q/s}$  [27].

We aim for an axial ion separation of around  $5 \mu\text{m}$  which, for  $^{40}\text{Ca}^+$  ions means a trapping potential of  $\omega_z \approx 2\pi \cdot 1.6 \text{ MHz}$ . This ion separation was chosen to reduce the cross talk between ions when singly addressed (see section 3.5).

We are targeting approximately 5 MHz for our radial frequencies, as we shall use radial addressing for two-qubit entangling gates. The choice of this higher frequency is motivated by several factors. The Doppler cooling limit ( $\bar{n} = \Gamma/\omega$ , where  $\Gamma$  is the transition linewidth and  $\omega$  is the frequency of the cooled mode) inversely scales with the mode frequency. Consequently, higher mode frequencies result in lower temperatures following initial cooling. Additionally, a higher center-of-mass radial mode enables greater frequency separation of radial modes in a multi-ion crystal, which allow for greater selectivity of participating modes.

Using the pseudopotential approximation [34] for the confining field, we can find a trapping frequency in one radial direction  $\omega_p$

$$\omega_p = \frac{e\alpha V_{RF}}{\sqrt{2}\Omega_{RF}M\rho^2}, \quad (1)$$

where  $\alpha$  is a factor of order unity given by the geometry of the trap,  $V_{RF}$  and  $\Omega_{RF}$  are the voltage and frequency provided to the RF-electrode,  $M$  is the mass of the ion, and  $\rho$  is the ion-RF electrode separation. Applying some DC voltage on the axial electrodes leads to axial confinement with frequency  $\omega_{ax}$ , but must defocus the radial confinements as the total curvature of the pseudopotential must remain constant,

$$\omega_{rad} = \sqrt{\omega_p^2 - \omega_{ax}^2/2}. \quad (2)$$

Unlike the macroscopic blade trap, the NPL trap focuses one of the radial modes and defocuses the other when the DC electrodes are increased due to the “cross” arrangement of DC and RF electrodes, Figure 3 (c),

$$\omega_{rad\pm} = \sqrt{\omega_p^2 - (1 \mp \beta)\omega_{ax}^2/2}, \quad (3)$$

where  $\beta$  is some factor due to the geometry of this cross arrangement. From simulation  $\beta > 1$  for  $\Omega_{RF} = 2\pi \cdot 23$  MHz and  $V_{RF} = 200$  V and so one radial mode increases with DC voltage applied and one decreases. A possible set of parameters to achieve

	$V_{RF}/V$	$V_{DC}/V$	$\Omega_{RF}/(2\pi \cdot \text{MHz})$	$\omega/(2\pi \cdot \text{MHz})$		q
				$\omega_{ax}$	$\omega_{rad}$	
Experiment	200	-7	23	1.6	4.9	0.61
Loading	100	-2	23	0.8	2.0	0.25

**Table 2.** Simulated parameters for both “Experiment” and “Loading” settings  $^{40}\text{Ca}^+$  with the NPL trap.

$\omega_{ax} = 2\pi \cdot 1.6$  MHz and  $\omega_{rad+} = 2\pi \cdot 4.9$  MHz can be seen on the “Experiment” trapping in table 2.

XX remove XX From Mathieu equations, stable trapping exists for  $q < 0.9$  [35], where  $q = 2\sqrt{2}\omega/\Omega_{RF}$ , however convenient trapping of hot ions requires  $q$  to be as low as possible.



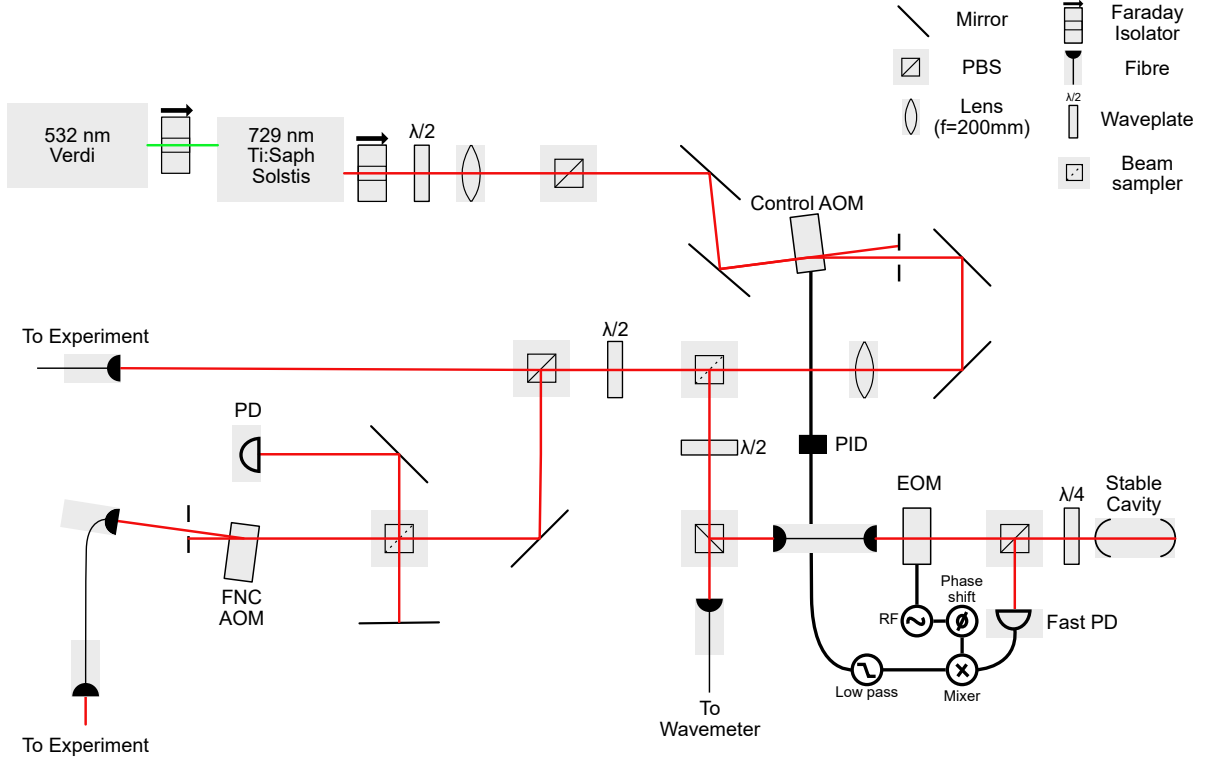


**Figure 4.** The 729-nm system being constructed for use in the “FastGates” experiment. A Ti:Saph laser tuned to 729-nm is pumped by a 532-nm source. Light is picked off at the first beam sampler to stabilise by PDH locking to a cavity.

To satisfy this requirement a “Loading” setting (with parameters in table 2) may be used with  $q = 0.25$  and then the  $V_{RF}$  ramped to the “Experiment” trapping for high radial mode frequencies.

### 3.3. Laser systems

Lasers are a key tool for creating the highly localised, strong electric field amplitudes and gradients needed to drive both carrier and sideband transitions of the trapped ion. As shown in Figure 2, we will use the levels  $4S_{1/2}$  to  $3D_{5/2}$  with a 729-nm quadrupole transition to define our qubit. Therefore the 729-nm laser is used to implement single- and multi-qubit gates. We also use this transition, after Doppler cooling, for resolved sideband cooling to bring the motional mode close to its ground state.

This laser must be narrow linewidth ( $\Gamma < 1$  Hz), and for fast gates we require large electric-field intensities at the ion to drive sideband transitions due to a low Lamb-Dicke factor for the 729-nm transition. Pumped Ti:Saph laser systems have been shown to be both relatively high power and narrow linewidth, making them suitable for our experiment.

We pump an M2 Solstis Ti:Saph with 15 W of 532-nm light from a Verdi system to produce around 4W of 729-nm light. A schematic of the 729-nm system being built

is shown in Figure 4. The frequency is stabilized by the Pound-Drever-Hall (PDH) technique with a high finesse cavity. PDH locking requires taking the laser light and applying two sidebands via an electro-optical modulator (EOM). This phase modulated light is then directed onto a stable cavity and a reflected signal is directed onto a fast photodetector. The reflection from the cavity consists of the interference between the carrier and the sidebands which have been respectively altered by the cavity transfer function. The photodetector signal is mixed down with the same oscillator signal as provided to the EOM but delayed by some chosen phase, and finally low pass filtered to produce a signal for use as the error signal in the servo loop. This error gives a measure for how far the carrier frequency is from the stable cavity resonant frequency and is used for feedback onto the control AOM situated after the Solstis.

Some of the 729-nm light is picked off and sent to a wavemeter to monitor the frequency. However, the majority is coupled to two output fibres for our experiment and another within the group. We transport the 729-nm light from a dedicated laser lab to a room containing the trap apparatus by a 10 m single mode polarization maintaining. To remove the phase noise introduced by mechanical and thermal effects in the fibre we implement fibre noise cancellation.

### *3.4. Inside the vacuum*

Here, we describe the instrumentation required, and being constructed, for decoupling the ion from any unwanted external environments. Our primary tools for this are working under Ultra High Vacuum (UHV) and surrounding the vacuum system with electromagnetic shielding. Inside the vacuum system we aim for a residual pressure of less than  $10^{-11}$  mbar. To reach this pressure, we must take care in material choice and thoroughly clean and bake all material within the vacuum system (a useful summary of tactics can be found in [36, 37]).

A schematic and photograph of the vacuum system can be seen in Figure 5. The system consists of an octagonal experimental chamber connected to an Ion pump, Ion Gauge and Ti:Sub pump. For optical access we have Dual CF100 viewports coated for 397-nm and 729-nm as well as two CF40 viewports coated for 397-nm, 422-nm, 729-nm, 854-nm and 866-nm.

We use in vacuum prisms to direct light onto the ions located within the slit of the NPL trap as there is no visibility of the ions from the side CF40 viewports and the high NA lens needed for single addressing obstructs the CF100 entry.

We use an electrical feedthrough on a CF40 flange to supply our trap chip with both DC and RF voltages. As the DC cables run within close proximity to the RF supply, electrical pick up is a potential issue within our DC lines. We mitigate this through a low pass filter board within close proximity of the trap chip.

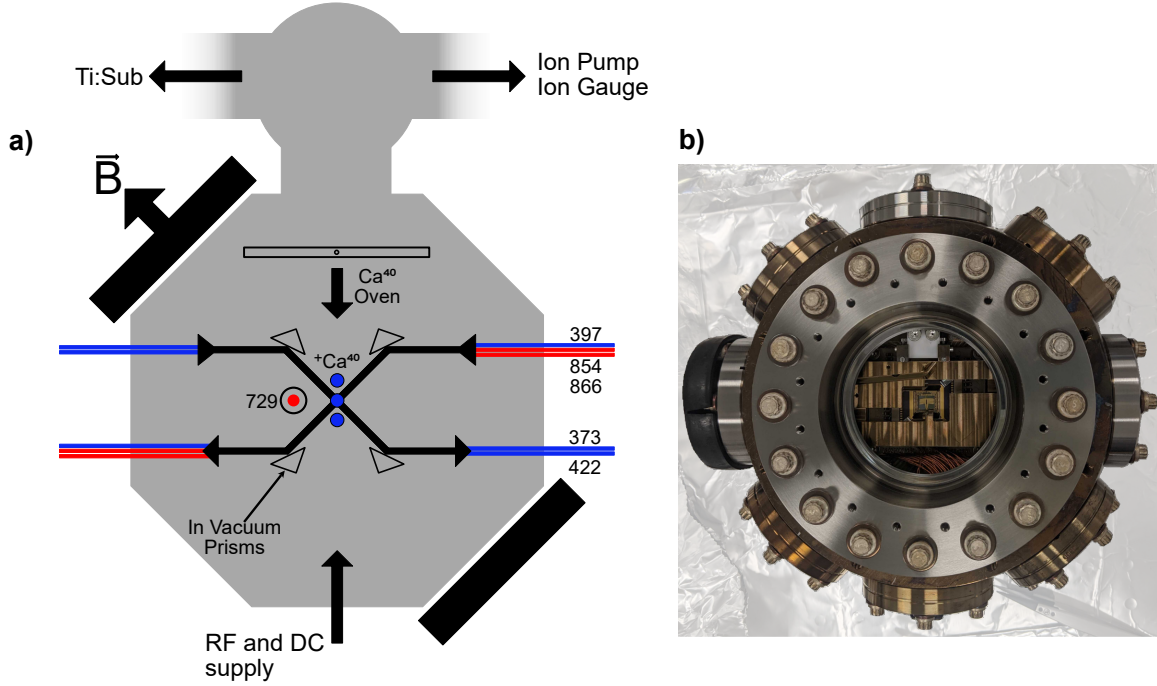


**Figure 5.** a) A schematic of the “FastGates” vacuum chamber. Wavelengths apart from 729-nm enter through the side CF40 viewports and are directed onto the ions by in vacuum prisms. The 729-nm light enters through the larger CF100 viewports. b) A photograph of the assembled system prior to baking.

### 3.5. Single Addressing

A unique feature of our system is the ability to produce standing wave single ion addressing. The design of this system is shown in Figure 6. A single ion addressing system must be able to illuminate selected ions in the crystal whilst the others remain unperturbed. The advantage of single addressing, other than ion selectivity, is the intensity of light due to the tight waist as the ion location. This high intensity will enable a greater SDF and thus faster gates.

Our ions are separated by a distance  $d \approx 5 \mu\text{m}$ . For an ideal Gaussian beam waist radius of the  $\omega_0 = 1 \mu\text{m}$ , the Electric field intensity cross talk to a neighbouring ion will be  $1 \times 10^{-11}$ . To produce this beam waist we must ensure we are not diffraction limited. Focussing a collimated beam with an objective lens of 0.6 onto the ion provide  $\omega_0 = 386 \text{ nm}$  for  $\lambda = 729\text{-nm}$  light. The lens edges diffract the spots and aberrations present in real optical components cause our spot to be non-gaussian and increase the cross talk seen at the neighbouring ions. Therefore care is taken in the optical design.

To illuminate selected ions we steer an input beam using Acousto-Optical-Deflectors (AODs) [38–40], where the angle deflected is proportional to the drive frequency supplied

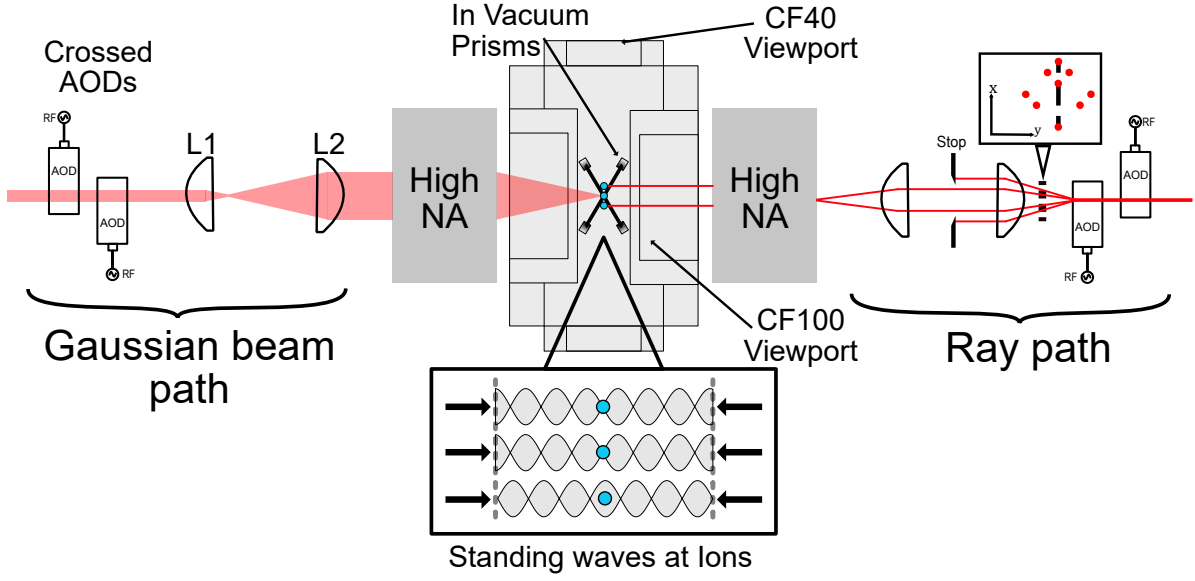


**Figure 6.** The standing wave single addressing system. Dual high NA objectives focus the light to a tight waist at the ions location. AODs are used to steer the light to only selected ions. The left hand side of the figure shows the Gaussian profile of the light, whilst the right hand side shows a ray representation of how two singly addressing spots are formed at the ions. L1 is a telecentric scanning lens and in combination with L2 form a beam expander.

to the AOD. Multiple output beams can be formed by supplying multiple RF tones to the AOD. We require the beam wave vectors to be parallel with the radial mode direction of the ion crystal. This requirement ensures that we drive motion on the radial modes exclusively. Therefore after the AODs we convert this angular separation of beams to distance separation using a telecentric scan lens (Figure 6 L1). This scan lens and L2 form a telescope to expand the beam before the high NA objective.

This single addressing system is implemented on both sides of the UHV chamber to form counter-propagating beams at the ion location. AODs are an ideal choice for creating standing wave as the location the waist is formed along the ion chain can be finely tuned by varying the AOD RF drive. Furthermore, the phases of two beams formed by the AODs can be controlled independently by varying the phases of the respected RF drives. This allows control over the phase of each singly addressed standing wave.

#### 4. Conclusion

We presented experimental results for using standing waves to implement Mølmer-Sørensen entangling gates where errors due to the carrier term are suppressed. These experiments were conducted using a previous apparatus, which served as a platform for proof-of-principle work. However, this setup has inherent limitations related to gate duration due to laser power availability and the constraint of global ion addressing.

Therefore, a new ion trap apparatus, with the unique capability of single ion addressing using standing waves, is described and design choices are motivated. This system will allow further studies on high fidelity fast entangling operations which are a critical component of realizing a useful NISQ device.

## 5. Outlook

We have fully assembled the trap chamber and it is ready to be placed in the trapping laboratory. Beam paths for 397-nm, 854-nm, 866-nm and the PI system are completed.

In the next 6 months we will build up the optics around the trap chamber to direct light onto the ions and build up control hardware and software for trapping. We should be able to trap at this point and start to characterize our system and calibrate the trapping to reduce micromotion.

Further we will complete work on the 729-nm system which is currently delayed due to a faulty Verdi pump system. To characterize the 729-nm system we will benchmark the fidelity of single-qubit gates by globally addressing a single ion.

Once the system has an acceptable single-qubit error ( $\approx 1 \times 10^{-3}$ ), we will be ready to assemble the single ion addressing system described above. Standing wave single ion addressing on multi-ion chains would likely be a suitable topic for a technical paper on methods and to report on crosstalks and gate fidelities.

Work would then transition to implementing carrier suppressed MS gates on multi-ion crystals, replicating the results from the proof of principle experiments. Finally, the high intensity of light using the single addressing system will enable the exploration of entangling operations at a rate comparable to the motional mode frequencies of a multi-ion chain.

---

## References

1. Paul, W. Electromagnetic traps for charged and neutral particles. *Reviews of Modern Physics* **62**, 531–540 (1990).
2. Wineland, D. J. *et al.* Experimental Issues in Coherent Quantum-State Manipulation of Trapped Atomic Ions. *Journal of Research of the National Institute of Standards and Technology* **103**, 259–328 (1998).
3. Ludlow, A. D., Boyd, M. M., Ye, J., Peik, E. & Schmidt, P. O. Optical atomic clocks. *Reviews of Modern Physics* **87**, 637–701 (2015).
4. Blatt, R. & Roos, C. F. Quantum simulations with trapped ions. *Nature Physics* **8**, 277–284 (2012).
5. Ozeri, R. Tutorial: The trapped-ion qubit toolbox. *Contemporary Physics* **52**, 531–550 (2011).
6. Steane, A. M. Overhead and noise threshold of fault-tolerant quantum error correction. *Physical Review A* **68**, 042322 (2003).
7. Preskill, J. Quantum Computing in the NISQ era and beyond. *Quantum* **2**, 79 (2018).
8. Srinivas, R. *et al.* High-fidelity laser-free universal control of trapped ion qubits. *Nature* **597**, 209–213 (2021).
9. Ballance, C. J., Harty, T. P., Linke, N. M., Sepiol, M. A. & Lucas, D. M. High-Fidelity Quantum Logic Gates Using Trapped-Ion Hyperfine Qubits. *Physical Review Letters* **117**, 060504 (2016).
10. Harty, T. P. *et al.* High-Fidelity Preparation, Gates, Memory, and Readout of a Trapped-Ion Quantum Bit. *Physical Review Letters* **113**, 220501 (2014).
11. DiVincenzo, D. P. The Physical Implementation of Quantum Computation. *Fortschritte der Physik* **48**, 771–783 (2000).
12. Blatt, R. & Wineland, D. Entangled states of trapped atomic ions. *Nature* **453**, 1008–1015 (2008).
13. Ono, T., Okamoto, R. & Takeuchi, S. An entanglement-enhanced microscope. *Nature Communications* **4**, 2426 (2013).
14. Nichol, B. C. *et al.* An elementary quantum network of entangled optical atomic clocks. *Nature* **609**, 689–694 (2022).
15. Sorensen, A. & Molmer, K. Entanglement and quantum computation with ions in thermal motion. *Physical Review A* **62**, 022311 (2000).
16. Schäfer, V. M. *et al.* Fast quantum logic gates with trapped-ion qubits. *Nature* **555**, 75–78 (2018).
17. Schäfer, V. M. Fast Gates and Mixed-Species Entanglement with Trapped Ions. *Ph.D. thesis, University of Oxford* (2020).
18. Saner, S. *et al.* Breaking the entangling gate speed limit for trapped-ion qubits using a phase-stable standing wave. *arXiv*, 2305.03450 (2023).

19. Thirumalai, K. High-fidelity mixed species entanglement of trapped ions. *Ph.D. thesis, University of Oxford* (2019).
20. Knill, E. *et al.* Randomized benchmarking of quantum gates. *Physical Review A* **77**, 012307 (2008).
21. Magesan, E., Gambetta, J. M. & Emerson, J. Scalable and Robust Randomized Benchmarking of Quantum Processes. *Physical Review Letters* **106**, 180504 (2011).
22. Hughes, A. C. Benchmarking memory and logic gates for trapped-ion quantum computing. *Ph.D. thesis, University of Oxford* (2021).
23. Barton, P. A. *et al.* Measurement of the lifetime of the 3d 2D5/2 state in  $^{40}\text{Ca}^+$ . *Physical Review A* **62**, 032503 (2000).
24. Nadlinger, D. P. Device-independent key distribution between trapped-ion quantum network nodes. *Ph.D. thesis, University of Oxford* (2022).
25. Nichol, B. C. An elementary quantum network of entangled optical atomic clocks. *Ph.D. thesis, University of Oxford* (2022).
26. Woodrow, S. Linear Paul trap design for high-fidelity, scalable quantum information processing. *MSc. thesis, University of Oxford* (2016).
27. Choonee, K., Wilpers, G. & Sinclair, A. G. Silicon microfabricated linear segmented ion traps for quantum technologies. *19th Int. Confrence on Solid-State Sensors*, 615–618 (2017).
28. Allcock, D. Surface-electrode ion traps for scalable quantum computing. *Ph.D. thesis, University of Oxford* (2011).
29. Kielpinski, D., Monroe, C. & Wineland, D. J. Architecture for a large-scale ion-trap quantum computer. *Nature* **417**, 709–711 (2002).
30. Turchette, Q. A. *et al.* Heating of trapped ions from the quantum ground state. *Physical Review A* **61**, 063418 (2000).
31. Maunz, P. *High Optical Access Trap 2.0*. tech. rep. SAND–2016-0796R, 1237003, 618951 (2016), 10.2172/1237003.
32. See, P., Wilpers, G., Gill, P. & Sinclair, A. G. Fabrication of a Monolithic Array of Three Dimensional Si-based Ion Traps. *Journal of Microelectromechanical Systems* **22**, 1180–1189 (2013).
33. Wilpers, G., See, P., Gill, P. & Sinclair, A. G. A monolithic array of three-dimensional ion traps fabricated with conventional semiconductor technology. *Nature Nanotechnology* **7**, 572–576 (2012).
34. Madsen, M., Hensinger, W., Stick, D., Rabchuk, J. & Monroe, C. Planar ion trap geometry for microfabrication. *Applied Physics B* **78**, 639–651 (2004).
35. Berkeland, D. J., Miller, J. D., Bergquist, J. C., Itano, W. M. & Wineland, D. J. Minimization of ion micromotion in a Paul trap. *Journal of Applied Physics* **83**, 5025–5033 (1998).
36. Birnbaum, K. M. Ultra-High Vacuum Chambers. *Useful Notes* (2005).

37. Wolf, J. Cryogenic, near-field quantum logic chips with passive field nulling on  $^{43}\text{Ca}^+$ . *Ph.D. thesis, University of Oxford* (2019).
38. Nagourney, W. Quantum Electronics for Atomic Physics and Telecommunication. *Oxford University Press* (2014).
39. Li, R.-R. *et al.* A low-crosstalk double-side addressing system using acousto-optic deflectors for atomic ion qubits. *arXiv*, 2306.01307 (2023).
40. Pogorelov, I. *et al.* Compact Ion-Trap Quantum Computing Demonstrator. *Physical Review X Quantum* **2**, 020343 (2021).



## 6. Appendix

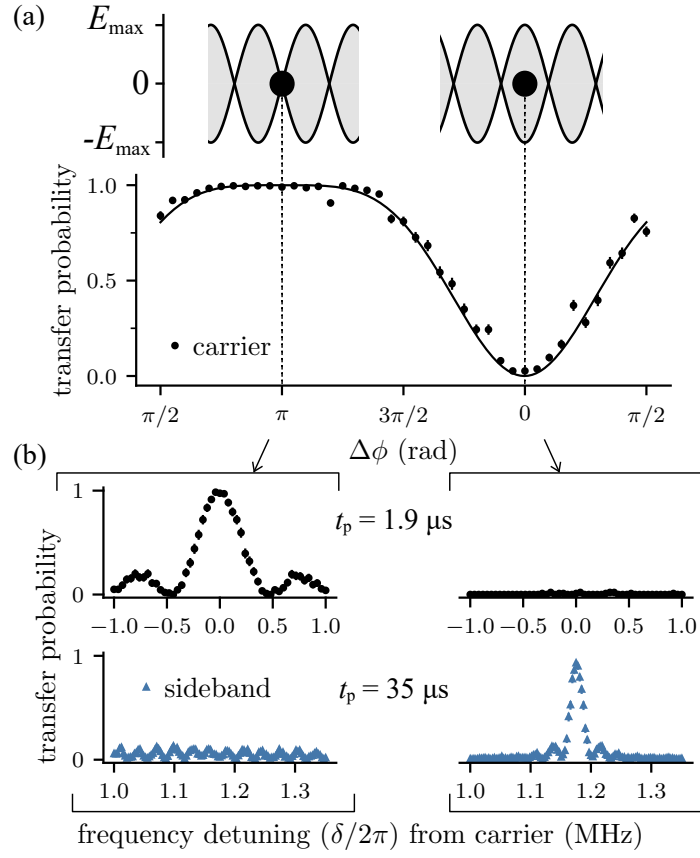


**Figure 7.** Single qubit gates using a standing wave (SW) for a quadrupole transition. The phase of the SW at the ion is given by  $\Delta\phi$ .  $\Delta\phi = 0$  corresponds to an E field antinode whilst  $\pi$  corresponds to a node. Carrier coupling is maximised at the node (max gradient) and suppressed at the antinode. Figure from [18].